Freewheeling current-based sensorless field-oriented control of Five-Phase PMSMs under IGBT failures of a single phase

Bing Tian, Marta Molinas, *Member, IEEE*, Quntao An, *Member, IEEE*,
Bo Zhou, Jiadan Wei, *Member, IEEE*

***Abstract*—Model-based sensorless field-oriented control (FOC) suffers from over-parameterization and can be laborious to use for a five-phase Permanent Magnet Synchronous Motor (5Φ-PMSM). On the other hand, Insulated Gate Bipolar Transistor (IGBT) frequently fails in an electric drive. Under IGBT failure, a freewheeling current is observed, and, above all, it carries the failed phase back-Electromotive Force (back-EMF) information. Based on this observation, this paper presents the design of a brand new sensorless FOC by exploiting the freewheeling current to accommodate both IGBT and position sensor failures, which is expected to further enhance the drive's fault-tolerant capability. The mathematical model of this current is firstly established to provide a theoretical basis and a comprehensive understanding of the presented sensorless FOC. By virtue of this model, a second-order generalized integrator with a frequency locked loop (SOGI-FLL) can be used as a simple and elegant way to extract position/speed estimates. Experimental results are provided to validate the proposed sensorless FOC philosophy.**

***Index Terms*—Sensorless field-oriented control, freewheeling current, SOGI-FLL, single-phase IGBT failure, five-phase PMSM**

I. Introduction

Nowadays, to accommodate the growing consumer demand for high-power density devices, the multi-phase motor has emerged and offers an alternative solution by increasing phase numbers. As such, the multi-phase drive has been nominated in the applications of the electric vehicle, aerospace, and electric propulsion to substitute its 3Φ counterparts [1-3]. On the other hand, the electric drive is frequently required to work in a very narrow space. To meet this working environment, the motor tends to pursue a compact physical structure with a trapezoidal back-Electromotive Force (back-EMF) and sometimes a reluctance torque [4, 5]. Besides, the multi-phase motor also offers additional merits like the fault-tolerant capability, because of the greater number of phases available. To date, there has been considerable research interest in improving the fault-tolerant capability of a five-phase (5Φ) motor at the failure of one or more phases [6]. As a summary, progress can be made from the perspectives of either the control algorithm design or motor structural design. The former is termed fault-tolerant control (FTC) and concentrates on the re-configuration of the remaining phase currents, whereas the latter is often referred to as fault-tolerant motor (FTM) [7]. The FTM is subject to a modular design for pursuing low mutual-inductances as well as huge self-inductances to restrain the short circuit current [8].

FTMs provide a balance of complexity and capability for implementing FTC [9, 10] which, however, suffers from poor compatibility with a generic 5Φ motor featured by the time-variant self- and mutual-inductances. In this regard, the investigation of a generic 5Φ Permanent Magnet Synchronous Motor (5Φ-PMSM) is more meaningful because of its general validity. FTC takes a variety of forms, however, the one under the field-oriented control (FOC) philosophy is more appealing. In this context, FTC manifests itself as the field-weakening control, maximum torque per ampere (MTPA), i_d=0 control, and torque ripple-free control as well as their combinations [11]. The fault-tolerant FOC of a generic 5Φ motor under certain phase failures relies on the decoupled modeling and the representative achievements are noted below. H. Guzman, [12], proposes a set of Clarke and Park transformations for a 5Φ induction motor under a single-phase open fault, and it proves the fault-tolerant FOC is possible. H. Zhou, [13], presents a remedial FOC for a 5Φ-FTM with constant self-inductances and low mutual-inductances. [11] finalizes a decoupled model for a generic 5Φ-PMSM under a single-phase open fault, and particularly, the inductances and rotor fluxes under the synchronous reference frame are constant.

The aforementioned decoupled models are most efficient under the open circuit fault. As per the relevant literature, the failures of motor windings and power converter are most common in an electric drive [14, 15]. As the first line of protection, shutdown of Insulated Gate Bipolar Transistors (IGBTs) is common in response to the electrical and thermal stress. Besides this, many severe faults, such as the short circuit, are also transformed into an open circuit fault by closing IGBTs at the first time of occurrence. Given this, the IGBT failure is the norm in an electric drive, irrespective of what the incipient faults involve. However, the IGBT failures do not create the desired open circuit situation, and to the best of our knowledge, this problem is only stressed in a few publications. As reported in [6, 16], an amount of current still circulates through the freewheeling diodes of the failed bridge, but no in-depth analysis is offered.

On the other hand, the failure of the position sensor is also hazardous to the FOC of a 5Φ drive. Regarding the position sensor fault detection, a common practice is to use a position observer to monitor the position sensor failure. Once a divergence between the measured position and the estimated one is observed, the control scheme switches to the sensorless control mode [17, 18]. Position sensor fault detection has been investigated in the previous articles, and this work does not attempt to cover this area in detail. In contrast, the sensorless control deserves more attention and can be grouped into four types: I) model-based sensorless FOC [19], II) high-frequency (HF) injection-based sensorless FOC [20], III) sensorless direct torque control (DTC) [21], and IV) zero sequence current/voltage-based sensorless FOC [22, 23]. In particular, an ultra HF-square-wave injection has recently emerged and claims a full speed range [24], however, the downgraded DC-bus voltage utilization is worthy of concern [25]. Besides this, Type-IV also features on the HF voltage/current injection, and its application is likewise limited to the low speed region [22, 23]. The dividing line between Types II and IV has been blurred, and Types I and II are more popular since FOC is always at the heart of the engineering practice. However, the sensorless control of a 5Φ drive is only reported in a few limited publications, currently, the following progress has been made. [25] proposes an HF injection-based sensorless FOC for a 5Φ-PMSM where the digital delay is incorporated; In [26], an ultra HF voltage injection from the 3rd harmonic space is attempted for a 5Φ-PMSM at a few hundred revolutions-per-minute (rpm). In [27], a robust back-EMF observer is presented for a 5Φ-PMSM under the single-phase open fault. As a major drawback, five extra phase-voltage sensors are needed to construct the state estimator. Besides, in [21], the sensorless DTC for the healthy condition is also investigated.

The sensorless FOC has been investigated for three decades and its application is typically found in household appliances like washing machines and air conditioners, where the mid-high speed performance is usually at the center of the attention. At present, the state-of-the-art method is the sliding mode observer-based sensorless FOC (SMO-sensorless-FOC) which claims strong robustness in estimating system states [28]. However, the back-EMF observer may not be as efficient as it appears. Advances are still being made to improve its steady-state performances, such as harmonic elimination of the estimated position [29], delayless filtering [28], inverter nonlinearity compensation [30], and its extension in the low-carrier-ratio areas [31]. Apart from this, an assumption of $\dot{\omega}=0$ and $\hat{\omega}=\omega$ is often made to linearize the back-EMF observer [27, 32], resulting in a restrained speed dynamic. The sensorless FOC of a 5Φ drive is normally borrowed from a 3Φ drive, and similar drawbacks are therefore inherited. Consequently, a completely new sensorless control is in demand to circumvent these defects of the model-based methods.

Although the position sensor and IGBT failure rarely occur simultaneously, they can occur successively. For the first time, this work combines the IGBT failure with position sensor failure to further enhance the fault-tolerant capability of an electric drive. To this end, this paper investigates a brand-new sensorless control by exploiting an existing current sensor to substitute the software back-EMF observer. It is found experimentally that an amount of current circulates through the anti-parallel diodes of the failed bridge which carries the back-EMF signal; however, currently, no related articles reveal the modeling of this current, and this work attempts to fill this gap. In post-fault, the 5Φ-PMSM downgrades to a 4Φ-motor fed by a 4Φ-inverter with the failed bridge serving as a zero-sequence path, thus the freewheeling current is termed “zero-sequence current”. This zero-sequence current reflects the failed phase’s back-EMF state and thus eliminates the need for a software back-EMF observer which suffers over-parameterization and a slow dynamic. To extract speed and position estimates from the freewheeling current, a second-order generalized integrator (SOGI) with a frequency locked loop (FLL) is adopted because of the simplicity it offers. For comparative purposes, a complex-valued model of an SMO-sensorless-FOC is established by incorporating parameter and speed mismatches. This complex-valued model suggests the system is prone to oscillation under some disturbances because of its slow dynamic. Fortunately, there is no such issue with the presented method, benefiting from an improved dynamic. The experimental comparisons confirm the stated advantages. Meanwhile, the anti-disturbance of the proposed method in response to external/internal disturbances is also evaluated.

The novelty of this work lies in the freewheeling current modeling and its first attempt at the sensorless FOC by using this current. Compared with the widely investigated SMO-sensorless-FOC which is often criticized for its slow dynamic and over-parameterization, the presented sensorless FOC achieves: (1) an improved dynamic with decent accuracy, and (2) less parameterization. As an added value, the freewheeling current modeling enriches the decoupled control theory of a 5Φ-PMSM subjected to the IGBT failure which is a norm in an electric drive. As a major drawback, the presented sensorless FOC is limited to the single-phase IGBT-failure condition only.

II. Freewheeling Current Modeling

A. *Analysis of IGBT failure*

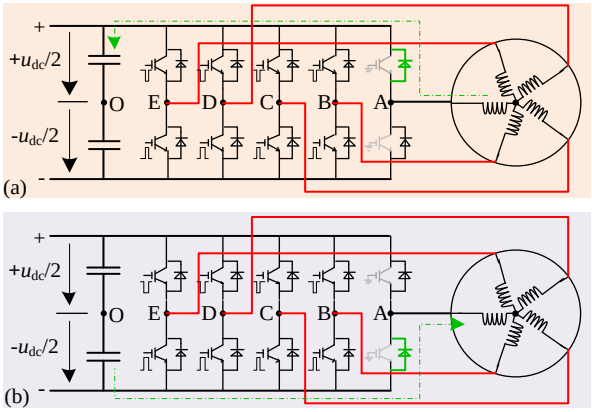

Fig.1 Freewheeling current through a) the upper diode, and b) the lower diode.

Without loss of generality, suppose the gating signals of phase-A IGBTs are grounded to protect the motor from possible

secondary damage. The topology of a 5Φ drive under phase-A IGBT failure is illustrated in Fig.1, where the inactive phase winding is still connected to the power stage. Even though the electrical faults are manifold in an electric drive, they are primarily transformed into the IGBT failures by the gate driver. Hence, the IGBT failure can be the norm, regardless of the incipient faults. However, the motor is not open circuited, and, as pointed out by [16], a certain current still circulates through the anti-parallel diodes of the failed bridge.

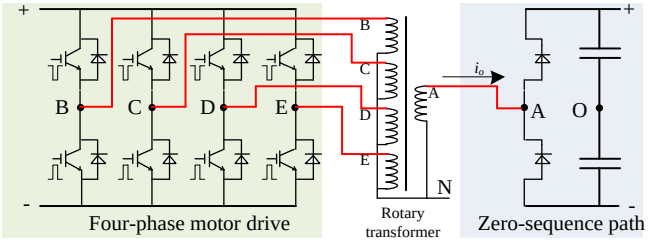

Fig.2 Re-definition of the electric drive at the failure of phase-A IGBTs.

For simplicity, the stator windings are divided into two sets: 1) the primary set comprises four healthy windings fed by the four healthy bridges, and 2) the other set involves only the inactive winding which is physically connected to the mid-point of the failed bridge. Fig.2 re-defines this faulty electric drive where the inactive winding is treated as a zero-sequence path. For a generic 5Φ-PMSM, the stator windings are magnetically linked, and this effect is manifested as mutual-inductances. In Fig.2, a rotary transformer is used to demonstrate the magnetic coupling effect. In this work, a four-phase five-bridge (4Φ5B) inverter concept is introduced to gain a better understanding of the freewheeling current.

The mathematic model for the inactive phase is given by

$$u_{\mathrm{AN}} = r_s i_{\mathrm{A}} + \frac{\mathrm{d}}{\mathrm{d}t}\left(L_{\mathrm{AA}} i_{\mathrm{A}} + L_{\mathrm{AB}} i_{\mathrm{B}} + L_{\mathrm{AC}} i_{\mathrm{C}} + L_{\mathrm{AD}} i_{\mathrm{D}} + L_{\mathrm{AE}} i_{\mathrm{E}}\right) + e_{\mathrm{A}} \quad (1)$$

where u_{xN} with x=A,B,C,D,E stands for the terminal-to-neutral voltage on phase-x (also known as the phase voltage), i_x with x=A,B,C,D,E denotes the phase current whose positive direction is defined as flowing into the neutral point (denoted as "N" point), r_s is the stator resistance, L_{xy} with x,y=A,B,C,D,E refers to the self- or mutual inductances, and e_x with x=A,B,C,D,E represents the back-EMF of phase-x.

Whereas the remaining phase voltages are represented by

$$\begin{bmatrix} u_{\mathrm{BN}} \\ u_{\mathrm{CN}} \\ u_{\mathrm{DN}} \\ u_{\mathrm{EN}} \end{bmatrix} = r_s \begin{bmatrix} i_{\mathrm{B}} \\ i_{\mathrm{C}} \\ i_{\mathrm{D}} \\ i_{\mathrm{E}} \end{bmatrix} + \frac{\mathrm{d}}{\mathrm{d}t}\left(\begin{bmatrix} L_{\mathrm{BB}} & L_{\mathrm{BC}} & L_{\mathrm{BD}} & L_{\mathrm{BE}} \\ L_{\mathrm{CB}} & L_{\mathrm{CC}} & L_{\mathrm{CD}} & L_{\mathrm{CE}} \\ L_{\mathrm{DB}} & L_{\mathrm{DC}} & L_{\mathrm{DD}} & L_{\mathrm{DE}} \\ L_{\mathrm{EB}} & L_{\mathrm{EC}} & L_{\mathrm{ED}} & L_{\mathrm{EE}} \end{bmatrix} \begin{bmatrix} i_{\mathrm{B}} \\ i_{\mathrm{C}} \\ i_{\mathrm{D}} \\ i_{\mathrm{E}} \end{bmatrix} \right) + \begin{bmatrix} e_{\mathrm{B}} \\ e_{\mathrm{C}} \\ e_{\mathrm{D}} \\ e_{\mathrm{E}} \end{bmatrix} + \frac{\mathrm{d}}{\mathrm{d}t} \begin{bmatrix} L_{\mathrm{BA}} i_{\mathrm{A}} \\ L_{\mathrm{CA}} i_{\mathrm{A}} \\ L_{\mathrm{DA}} i_{\mathrm{A}} \\ L_{\mathrm{EA}} i_{\mathrm{A}} \end{bmatrix} \quad (2)$$

For a single-phase open fault, i_A is null so the last term of (2) is zero. In the former articles, a set of reduced-order Clarke and Park matrices is presented which is capable to translate (2) into DC quantities. On this basis, this paper enriches the decoupled modeling theory by incorporating the freewheeling current.

The reduced-order Clarke and Park matrices for the single-phase open fault case are given by

$$\left[\mathbf{T}_{\mathrm{pk}}\right] = \begin{bmatrix} \cos\theta & \sin\theta & 0 & 0 \\ -\sin\theta & \cos\theta & 0 & 0 \\ 0 & 0 & 1 & 0 \\ 0 & 0 & 0 & 1 \end{bmatrix} \quad (3)$$

$$\left[\mathbf{T}_{\mathrm{clk}}\right] = \frac{2}{5}\begin{bmatrix} \cos\delta - 1 & \cos 2\delta - 1 & \cos 3\delta - 1 & \cos 4\delta - 1 \\ \sin\delta & \sin 2\delta & \sin 3\delta & \sin 4\delta \\ \sin 3\delta & \sin 6\delta & \sin 9\delta & \sin 12\delta \\ 1 & 1 & 1 & 1 \end{bmatrix} \quad (4)$$

with δ=2π/5 the spatial angle between adjacent windings.

Accordingly, the decoupled model under phase-A open fault can be given by

$$\begin{bmatrix} u_{\mathrm{d}} \\ u_{\mathrm{q}} \\ u_{\mathrm{q3}} \end{bmatrix} = r_s \begin{bmatrix} i_{\mathrm{d}} \\ i_{\mathrm{q}} \\ i_{\mathrm{q3}} \end{bmatrix} + \begin{bmatrix} L_{\mathrm{d}} & 0 & 0 \\ 0 & L_{\mathrm{q}} & 0 \\ 0 & 0 & L_{\mathrm{q3}} \end{bmatrix} \frac{d}{dt} \begin{bmatrix} i_{\mathrm{d}} \\ i_{\mathrm{q}} \\ i_{\mathrm{q3}} \end{bmatrix} - \omega \begin{bmatrix} 0 & L_{\mathrm{q}} & 0 \\ -L_{\mathrm{d}} & 0 & 0 \\ 0 & 0 & 0 \end{bmatrix} \begin{bmatrix} i_{\mathrm{d}} \\ i_{\mathrm{q}} \\ i_{\mathrm{q3}} \end{bmatrix} + \omega \begin{bmatrix} 0 \\ \lambda_{\mathrm{r1}} \\ 3\lambda_{\mathrm{r3}} \cos 3\theta \end{bmatrix} \quad (5)$$

where u_d, u_q, u_{q3} are the d-q-q_3 frame voltages; i_d, i_q, i_{q3} are the d-q-q_3 frame currents; L_d, L_q, L_{q3} are the d-q-q_3 frame inductances which are constant, with their detailed representations referred to [11]; λ_{r1}, λ_{r3} are the magnitudes of 1st and 3rd rotor flux linkages; and ω is the rotor speed (electrical).

Under bridge-A failure, i_A is small and its influence on the FOC is limited and can be offset by the resonant controllers. This implies that the decoupled model also applies to the IGBT failure condition.

The electromagnetic torque under the open fault is given by

$$T_e = \frac{5p}{2}\left[i_d i_q (L_d - L_q) + i_q \lambda_{r1}\right] + \frac{5p\lambda_{r3}}{2}\left[3i_{q3} + \frac{3(i_d \sin 2\theta + i_d \sin 4\theta - i_q \cos 2\theta + i_q \cos 4\theta)}{2}\right] \quad (6)$$

where T_e is the electromagnetic torque, and p represents the number of pole pairs.

Since i_A carries the back-EMF information, the modeling of i_A (or rather, the freewheeling current) is primarily performed, which constitutes one of the main contributions in this work.

B. Modeling of zero-sequence voltage

For a 5Φ-PMSM with undamaged windings, one always has

$$u_{\mathrm{AN}} + u_{\mathrm{BN}} + u_{\mathrm{CN}} + u_{\mathrm{DN}} + u_{\mathrm{EN}} \equiv 0 \quad (7)$$

$$u_{\mathrm{XN}} \equiv u_{\mathrm{XO}} - u_{\mathrm{NO}},\ x = A,B,C,D,E \quad (8)$$

where u_{NO} denotes zero-sequence voltage measured between point "N" and DC bus midpoint (denoted as "O" point).

Substituting (8) into (7) yields

$$5u_{\mathrm{NO}} = u_{\mathrm{AO}} + \left(u_{\mathrm{BO}} + u_{\mathrm{CO}} + u_{\mathrm{DO}} + u_{\mathrm{EO}}\right) \quad (9)$$

where u_{AO}, u_{BO}, u_{CO}, u_{DO}, u_{EO} are pole voltages measured between motor terminals and point "O". Note that the pole voltages are not identical to the phase voltages in this scenario, and this problem has been addressed in [33].

The pole voltages of the active phases can be modeled as

$$\begin{cases} u_{\mathrm{BO}} = u_{dc} s_B - 0.5u_{dc} \\ u_{\mathrm{CO}} = u_{dc} s_C - 0.5u_{dc} \\ u_{\mathrm{DO}} = u_{dc} s_D - 0.5u_{dc} \\ u_{\mathrm{EO}} = u_{dc} s_E - 0.5u_{dc} \end{cases} \quad (10)$$

where s_x with x=B,C,D,E denotes the switching status of the

upper IGBT.

Whereas u_{AO} is modeled as a current-controlled voltage-source (CCCV), and its representation is given below, ignoring the diode forward voltage

$$u_{\mathrm{AO}}=\frac{u_{dc}}{2}sign(i_o)=\begin{cases}0.5u_{dc}, & if\ i_o\succ 0\\ 0, & if\ i_o=0\\ -0.5u_{dc}, & if\ i_o\prec 0\end{cases} \tag{11}$$

where i_o is the freewheeling current also termed "zero-sequence current" from the perspective of the 4Φ5B inverter.

This CCCV takes the following form

$$u_{\mathrm{AO}}=r_o i_o,\quad r_o=\frac{u_{dc}}{2|i_o|} \tag{12}$$

where r_o denotes the control gain of the CCCV and manifests itself as a resistor. r_o is infinite when the following property is satisfied

$$r_o\Big|_{i_o\in(-\gamma,\gamma)}=\frac{u_{dc}}{2|i_o|}=+\infty \tag{13}$$

with γ denoting the maximum value of i_o.

As γ is much smaller than the rated current, condition (13) always holds. On the other hand, due to the inverter's physical limit, the maximum value of u_{AO} is firmly restricted between $\pm½u_{\mathrm{dc}}$, thereby (12) makes sense in describing a faulty inverter.

Substituting (9) with (10) and (12), u_{NO} can be derived as

$$u_{\mathrm{NO}}=\frac{1}{5}u_{\mathrm{AO}}+\frac{4}{5}\left[\frac{u_{dc}}{4}\left(s_B+s_C+s_D+s_E\right)-\frac{1}{2}u_{dc}\right]=\frac{1}{5}r_o i_o+\frac{4}{5}u_{CMV} \tag{14}$$

where

$$u_{CMV}=\frac{u_{dc}}{4}\left(s_B+s_C+s_D+s_E\right)-\frac{1}{2}u_{dc} \tag{15}$$

In (14) and (15), u_{CMV} stands for the common-mode voltage (CMV) because of the inverter chopping, and it has a zero-mean.

C. Modeling of the freewheeling current

For a 5Φ-PMSM, there exists

$$i_A+i_B+i_C+i_D+i_E\equiv 0 \tag{16}$$

In fault mode, the 5Φ drive downgrades to a 4Φ drive, with the failed winding acting as a zero-sequence path. Given this, we have

$$i_o=i_B+i_C+i_D+i_E=-i_A \tag{17}$$

Substitute (1) with (17), (1) is formalized as

$$\begin{aligned}&u_{\mathrm{AN}}=-r_s i_o+e_{\mathrm{A}}\\&+\frac{\mathrm{d}}{\mathrm{d}t}\left[\left(L_{\mathrm{AB}}-L_{\mathrm{AA}}\right)i_{\mathrm{B}}+\left(L_{\mathrm{AC}}-L_{\mathrm{AA}}\right)i_{\mathrm{C}}+\left(L_{\mathrm{AD}}-L_{\mathrm{AA}}\right)i_{\mathrm{D}}+\left(L_{\mathrm{AE}}-L_{\mathrm{AA}}\right)i_{\mathrm{E}}\right]\end{aligned} \tag{18}$$

The last term of (18) corresponds to the mutually induced voltage because of the magnetic coupling. Suppose i_d, i_q, i_{q3}, i_o are the motor currents represented under the d-q-q_3-o frame, then transform these currents into the stationary frame, we have

$$\left[i_{\mathrm{B}}\quad i_{\mathrm{C}}\quad i_{\mathrm{D}}\quad i_{\mathrm{E}}\right]=\left[\mathbf{T}_{\mathrm{clk}}\right]^{-1}\left[\mathbf{T}_{\mathrm{Pk}}\right]^{-1}\left[i_d\quad i_q\quad i_{q3}\quad i_o\right]^T \tag{19}$$

Substituting (19) into (18) yields

$$\begin{aligned}&\frac{\mathrm{d}}{\mathrm{d}t}\left(\left(L_{\mathrm{AB}}-L_{\mathrm{AA}}\right)i_{\mathrm{B}}+\left(L_{\mathrm{AC}}-L_{\mathrm{AA}}\right)i_{\mathrm{C}}+\left(L_{\mathrm{AD}}-L_{\mathrm{AA}}\right)i_{\mathrm{D}}+\left(L_{\mathrm{AE}}-L_{\mathrm{AA}}\right)i_{\mathrm{E}}\right)\\&=-\frac{d}{dt}\left[-2.5\left(L_m-L_\theta\right)i_d\cos\theta+2.5\left(L_m+L_\theta\right)i_q\sin\theta+2.5L_{ls}i_{\mathrm{o}}\right]\end{aligned} \tag{20}$$

where L_{ls} denotes the leakage inductance which is usually relatively small, L_m is the magnitude of the magnetizing inductance, and L_θ is the magnitude of the mutual inductance between the stator and rotor [11, 34].

Substituting (20) into (18) yields the following

$$\begin{aligned}&u_{\mathrm{NO}}=u_{\mathrm{AO}}-u_{\mathrm{AN}}\\&=r_o i_o+r_s i_o-e_{\mathrm{A}}+2.5L_{ls}\frac{\mathrm{d}i_{\mathrm{o}}}{\mathrm{d}t}+\frac{d}{dt}\left[-2.5\left(L_m-L_\theta\right)i_d\cos\theta+2.5\left(L_m+L_\theta\right)i_q\sin\theta\right]\end{aligned} \tag{21}$$

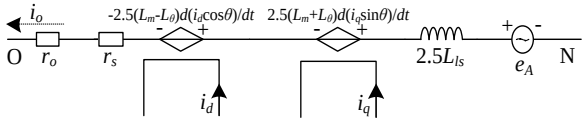

Fig.3 Graphical illustration of the zero-sequence path.

Fig.3 reveals the graphical form of the zero-sequence path. In this figure, the magnetic coupling is represented by two separate CCCVs which are directly controlled by i_d and i_q.

Combining (14) with (21) yields the following frequency-domain representation

$$\begin{aligned}i_{\mathrm{o}}=&\frac{e_{\mathrm{A}}+0.8u_{CMV}}{r_{\mathrm{s}}+0.8r_o+2.5sL_{ls}}\\&-\frac{\frac{d}{dt}\left[-2.5\left(L_m-L_\theta\right)i_d\cos\theta+2.5\left(L_m+L_\theta\right)i_q\sin\theta\right]}{r_{\mathrm{s}}+0.8r_o+2.5sL_{ls}}\end{aligned} \tag{22}$$

with

$$e_{\mathrm{A}}=-\omega\lambda_{r1}\sin\theta-3\omega\lambda_{r3}\sin 3\theta \tag{23}$$

Considering the following inequality which always holds

$$0.8r_o+r_{\mathrm{s}}\gg 2.5\omega L_{ls} \tag{24}$$

Equation (22) is rewritten as

$$\begin{aligned}i_{\mathrm{o}}=&\frac{e_{\mathrm{A}}}{r_{\mathrm{s}}+0.8r_o}+\frac{0.8u_{CMV}}{r_{\mathrm{s}}+0.8r_o}\\&-\frac{2.5\omega\left(L_m-L_\theta\right)\sin\theta}{r_{\mathrm{s}}+0.8r_o}i_d-\frac{2.5\omega\left(L_m+L_\theta\right)\cos\theta}{r_{\mathrm{s}}+0.8r_o}i_q\\&+\frac{2.5\left(L_m-L_\theta\right)\cos\theta}{r_{\mathrm{s}}+0.8r_o}\frac{di_d}{dt}-\frac{2.5\left(L_m+L_\theta\right)\sin\theta}{r_{\mathrm{s}}+0.8r_o}\frac{di_q}{dt}\end{aligned} \tag{25}$$

As per [11], L_d and L_q are represented by

$$L_d=L_{ls}+2.5\left(L_m-L_\theta\right),L_q=L_{ls}+2.5\left(L_m+L_\theta\right) \tag{26}$$

To minimize (25), we define

$$\begin{aligned}E_A^{ex}&=e_{\mathrm{A}}-2.5i_d\omega\left(L_m-L_\theta\right)\sin\theta-2.5\dot{i}_q\left(L_m+L_\theta\right)\sin\theta\\&=-\omega\lambda_{r1}^{ex}\sin\theta-3\omega\lambda_{r3}\sin 3\theta\end{aligned} \tag{27}$$

$$\lambda_{r1}^{ex}=\lambda_{r1}+i_d\left(L_d-L_{ls}\right)+\frac{\dot{i}_q}{\omega}\left(L_q-L_{ls}\right) \tag{28}$$

where E_A^{ex} and λ_{r1}^{ex} are the extended back-EMF and rotor flux which are borrowed from an SMO-sensorless-FOC. Note that λ_{r1}^{ex} is corrupted at the low speeds and thus the presented sensorless FOC is likewise unsuitable to the low speed region.

Substitute (26) and (27) into (25), this obtains

$$i_{\mathrm{o}}=\frac{E_A^{ex}}{r_{\mathrm{s}}+0.8r_o}+\frac{0.8u_{CMV}}{r_{\mathrm{s}}+0.8r_o}+\frac{\left(L_d-L_{ls}\right)\dot{i}_d-i_q\omega\left(L_q-L_{ls}\right)}{r_{\mathrm{s}}+0.8r_o}\cos\theta \tag{29}$$

where u_{CMV} is the high-frequency pulse, and this work uses a

double sampling technique to best restore the wanted signal i_o.

This paper firstly proposes a mathematical model for the freewheeling current. From (29), i_o directly reflects the back-EMF condition and can be used for the sensorless FOC. However, the back-EMF information can be affected by i_q and the dynamic of i_d, and below stresses the limitation of the presented sensorless FOC.

III. Proposed Sensorless Control scheme

A. The limitation of the proposed method

Equation (29) offers a brand-new way to perform the sensorless FOC by exploiting the freewheeling current which is by nature a good back-EMF estimator. The presented sensorless FOC is most efficient when: I) cosθ-related term in (29) is negligible, and II) λ_{r1}^{ex} is positive and stable.

To fulfill the first rule, we have

$$\left|\omega\lambda_{r1}^{ex}\right| \gg \left|\left(L_d - L_{ls}\right)\dot{i}_d - i_q\omega\left(L_q - L_{ls}\right)\right| \approx \left|i_q\omega\left(L_q - L_{ls}\right)\right| \quad (30)$$

The current i_d is subject to a slow dynamic either in the filed-weakening, or MTPA, or i_d=0 control mode, and the derivative of i_d is therefore disregarded. Correspondingly, i_q is supposed to satisfy the following property

$$i_q \ll \frac{\lambda_{r1}}{L_q - L_{ls}} = i_f \quad (31)$$

where i_f is defined as the excitation current due to the permanent magnet (PM). Note that i_f is considerable in many instances. For most motors with the current rating of around 1/5i_f, the phase shift while measuring E_A^{ex} is 11.3°. Ignore this minor phase shift, (29) can be approximated by

$$i_o = \frac{E_A^{ex}}{r_s + 0.8r_o} + \frac{0.8u_{CMV}}{r_s + 0.8r_o} \quad (32)$$

For some specific motors, the current rating can be up to 1/3i_f, and in this context, the position estimation error is expected 18.4°, and angle compensation is required, however, this topic is currently beyond the scope of this work.

On the other hand, from (28), λ_{r1}^{ex} is distorted because of the presence of i_d and i_q and becomes fluctuating when ω approaches zero, which means the sensorless FOC is unable to suit the low speed region. Theoretically, the low speed limit can be obtained by solving the following inequality

$$\lambda_{r1} + i_d\left(L_d - L_{ls}\right) \gg \left|\frac{\dot{i}_q}{\omega}\right|\left(L_q - L_{ls}\right) \quad (33)$$

As it is difficult to evaluate the magnitude of $\dot{i}_q$, the analytical value of the low speed limit is currently hard to give. However, according to the trials during the experiment, this low speed limit is roughly 350 rpm.

B. The adopted filtering technique

In practice, i_o is distorted and unable to follow a sinusoidal shape. In this case, band-pass filters (BPFs) are demanded prior to the position calculation. A SOGI is a good practice to extract the frequency of interest from i_o and it takes either of the following two forms [35, 36]

$$BPF_\alpha(s) = \frac{v_\alpha}{i_o} = \frac{k\omega s}{s^2 + k\omega s + \omega^2} \quad (34)$$

$$BPF_\beta(s) = \frac{v_\beta}{i_o} = \frac{k\omega^2}{s^2 + k\omega s + \omega^2} \quad (35)$$

with k the damping factor and ω the resonant frequency.

The graphical form of the SOGI-FLL is depicted in Fig.4, and it comprises two paralleled integrators which calculate v_α and v_β. Finally, v_α and v_β are forwarded to an FLL for the position/speed extraction.

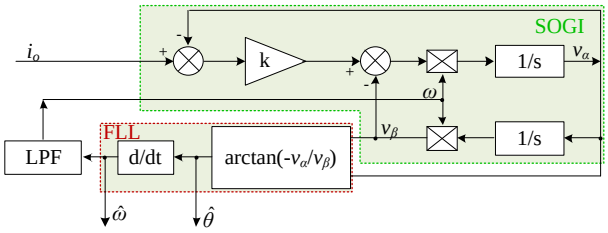

Fig.4 Graphical representation of the adopted SOGI-FLL.

The FLL takes broad forms, but the following algebraic operation is recommended

$$\hat{\theta} = \arctan\left(\frac{-v_\alpha}{v_\beta}\right), \quad \hat{\omega} = \frac{d\hat{\theta}}{dt} \quad (36)$$

The implementation of (36) is delayless and can be based on either the CORDIC (coordinate rotation digital computer) or a look-up table, both of which offer a fast speed dynamic with, however, a noisy profile. Nevertheless, this solution is still preferred as the electric drive is more complex than ever, and each observer shall be designed separately using a unique speed dynamic. The proposed sensorless FOC adopts this basic SOGI-FLL where the speed estimate is further processed before being used in other observers. The SOGI-FLL is not the innovation of this work and readers are referred to [36] for more details.

C. The proposed sensorless FOC

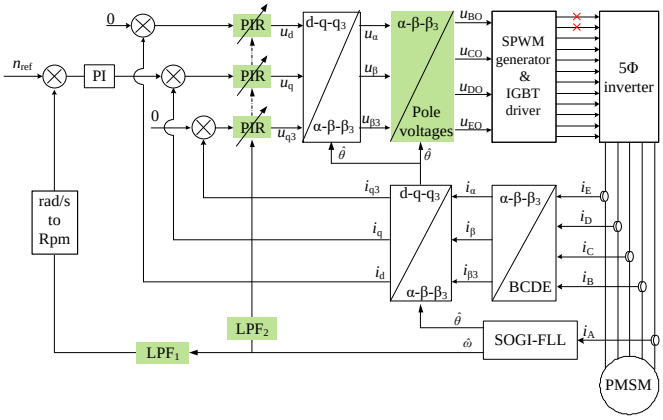

Fig.5 Overview of the adjustable speed drive under the IGBT failures using the proposed sensorless FOC.

Fig.5 outlines this adjustable speed drive under IGBT failures of a single-phase, using the proposed sensorless FOC. Aside from the Park and inverse Park transformations, other modules using the position or speed signals are marked in green and they are, respectively: 1) Proportional-Integral-Resonant (PIR) controllers to regulate d-q-q_3 frame currents; 2) the transformation of α-β-β_3 frame voltage to pole voltage, where

the failed phase back-EMF is required to offset the drifting neutral effect (refer to [33] for the details); and 3) low-pass filter #1 (LPF_1) and low-pass filter #2 (LPF_2) to smooth $\hat{\omega}$.

IV. Comparison With A Model-based Method

A. A model-based back-EMF observer

Sensorless control is mainly about back-EMF acquisition. In the proposed method, the back-EMF acquisition is based on an existing current sensor and robust to disturbances. However, in a model-based method, the back-EMF acquisition develops a closed-loop observer which can be conditionally stable. Take the SMO-sensorless-FOC as an example. In this method, similar quantities such as the extended rotor flux linkage and extended back-EMF can be defined below

$$\lambda_r^{ex} = \lambda_r + \left(L_\mathrm{d} - L_\mathrm{q}\right)\left(i_\mathrm{d} - \frac{\dot{i}_\mathrm{q}}{\omega}\right) \tag{37}$$

$$E_\alpha^{ex} = -\omega\lambda_{r1}^{ex}\sin\theta,\ E_\beta^{ex} = \omega\lambda_{r1}^{ex}\cos\theta \tag{38}$$

where λ_r^{ex} is the extended rotor flux linkage, and E_α^{ex} and E_β^{ex} are, respectively, the α- and β-axis extended back-EMFs.

From (37), the dynamic of i_q likewise impacts the extended rotor flux, especially at the low speeds. Although the extended back-EMFs defined in, respectively, (38) and (27), resemble each other, the way to acquire them differs. In a model-based method, a state estimator is developed which indirectly returns the back-EMF estimates. Before going into the state estimator, we define

$$i_{\alpha\beta} = i_\alpha + ji_\beta,\ u_{\alpha\beta} = u_\alpha + ju_\beta, E_{\alpha\beta}^{ex} = E_\alpha^{ex} + jE_\beta^{ex} \tag{39}$$

where $i_{\alpha\beta}$, $u_{\alpha\beta}$, and $E_{\alpha\beta}^{ex}$ are, respectively, the complex-valued current, voltage and extended back-EMF. Thereby, the matrix representation of the motor model can be minimized as a single-input single-output (SISO) system [27, 37]

$$sL_d i_{\alpha\beta} = -\left[R_\mathrm{s} - j\omega\left(L_\mathrm{d} - L_\mathrm{q}\right)\right]i_{\alpha\beta} + u_{\alpha\beta} - E_{\alpha\beta}^{ex},\ \omega = \frac{d\theta}{dt} \tag{40}$$

A state estimator is constructed below

$$s\hat{L}_d\hat{i}_{\alpha\beta} = -\left[\hat{R}_\mathrm{s} - j\hat{\omega}\left(\hat{L}_\mathrm{d} - \hat{L}_\mathrm{q}\right)\right]\hat{i}_{\alpha\beta} + u_{\alpha\beta} - \hat{E}_{\alpha\beta}^{ex},\ \hat{\omega} = \frac{d\hat{\theta}}{dt} \tag{41}$$

where the quantities with "^" indicate the estimated parameters. It has to be emphasized that $\hat{\omega}$ represents the prefiltered speed estimate according to the definition of the SISO system.

A saturation function-based sliding mode controller (SMC) is able to restrict the state estimation error onto the sliding surface. To facilitate the analysis, this SMC is simplified as a proportional component with an infinite gain

$$\hat{E}_{\alpha\beta}^{ex} = k_{smc}\left(\hat{i}_{\alpha\beta} - i_{\alpha\beta}\right) \tag{42}$$

where k_{smc} is the equivalent gain.

By solving the above three equations, we can obtain the representation of the complex-valued back-EMF estimate

$$\hat{E}_{\alpha\beta}^{ex} = \left(f_{u_{\alpha\beta}}(s)u_{\alpha\beta} + E_{\alpha\beta}^{ex}\right)f_{bEMF}(s) \tag{43}$$

with

$$f_{u_{\alpha\beta}}(s) = \frac{s\left(\hat{L}_d - L_d\right) + j\omega\left(L_\mathrm{d} - L_\mathrm{q}\right) - j\hat{\omega}\left(\hat{L}_\mathrm{d} - \hat{L}_\mathrm{q}\right) + \hat{R}_\mathrm{s} - R_\mathrm{s}}{s\hat{L}_d + \hat{R}_\mathrm{s} - j\hat{\omega}\left(\hat{L}_\mathrm{d} - \hat{L}_\mathrm{q}\right)} \tag{44}$$

and

$$f_{E_{\alpha\beta}}(s) = \frac{k_{smc}\left[s\hat{L}_d + \hat{R}_\mathrm{s} - j\hat{\omega}\left(\hat{L}_\mathrm{d} - \hat{L}_\mathrm{q}\right)\right]}{\left[s\hat{L}_d + \hat{R}_\mathrm{s} - j\hat{\omega}\left(\hat{L}_\mathrm{d} - \hat{L}_\mathrm{q}\right) + k_{smc}\right]\left[sL_d + R_\mathrm{s} - j\omega\left(L_\mathrm{d} - L_\mathrm{q}\right)\right]} \tag{45}$$

Equation (43) discloses the back-EMF estimate properties in the presence of parameter and speed mismatches. As per (43), $f_{u_{\alpha\beta}}(s)$ is a phase-lead compensator and introduces certain noises whereas $f_{E_{\alpha\beta}}(s)$ acts as a 2nd-order LPF.

B. Major drawbacks of the model-based method

From (43), $u_{\alpha\beta}$ contaminates $\hat{E}_{\alpha\beta}^{ex}$ via $f_{u_{\alpha\beta}}(s)$ and is therefore classified as a disturbance. This disturbance is expected to be fully attenuated by using well-matched parameters in the state estimator, however, this condition is too hard to fulfill.

Besides this, both poles and zeros of $f_{u_{\alpha\beta}}(s)$ and $f_{E_{\alpha\beta}}(s)$ can be time-variant (or rather, they vary with $\hat{\omega}$), and this indicates the state estimator tends to be nonlinear. To be specific $\hat{\omega}$ is prone to swinging under disturbances, and it aggravates the state estimator nonlinearity, which returns a more distorted back-EMF estimate. This distorted back-EMF estimate further generates an alternating $\hat{\omega}$, and, eventually, the state estimator becomes nonlinear. Therefore, the SMO-sensorless-FOC frequently assumes $\hat{\omega} = \omega$ and $\dot{\omega} = 0$ so that the poles and zeros can be time-invariant. Fortunately, the freewheeling current model makes no such assumption.

In summary, the SMO-sensorless-FOC is subject to a slow dynamic. In contrast, the back-EMF acquisition in the presented method takes advantage of an existing current sensor and is robust to the dynamic of $\hat{\omega}$. From this respect, the freewheeling current is more desirable to replicate the realistic back-EMFs.

C. Response time of the position estimate

As stressed earlier, i_o is sensed by an existing current sensor and not affected by the speed variation (or parameter mismatches). Up to this point, we only need to focus on the extraction of the position and speed estimates, and this can be accomplished with a single SOGI-FLL. Note that some SMO-sensorless-FOC also use the SOGI (or rather, BPF) for delayless filtering, and, from this perspective, the proposed method benefits from a reduced computational complexity for canceling a stator estimator.

From Fig.4, the natural frequency of a SOGI shall adapt the speed estimate, and the involved LPF is used to stabilize the natural frequency. The time constant of the LPF is set close or equal to the mechanical constant. However, this does not mean the natural frequency has to strictly follow the motor's actual

speed, and in fact, a certain speed mismatch is allowed.

Fig.6 reveals the bode plots of SOGIs with k=0.1,1,10, respectively. From Fig.6, the bandwidth of the SOGI is narrowed with a decrease of k. There are many criteria for choosing the SOGI's bandwidth, however, from a more practical viewpoint, k=1 can be a good trade-off as the inherent DC-bias during ADC sampling is not magnified along with a decent resiliency to the speed mismatch. Given this, the cut-off frequency of the SOGI is 1.5ω, and the response time for the position estimate is 1/1.5ω.

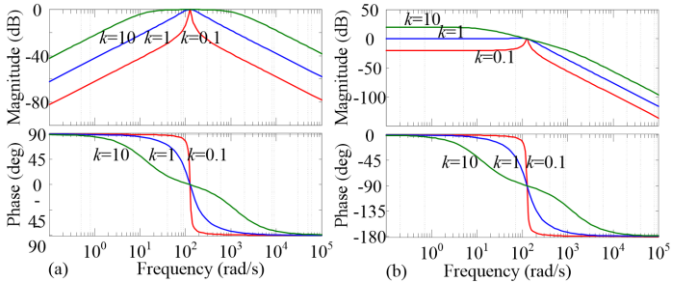

Fig.6 Bode plots of the SOGI under different damping factors. (a) The frequency response of $BPF_\alpha(s)$, and (b) the frequency response of $BPF_\beta(s)$.

V. Experimental Results

The proposed method is examined on a 5Φ-PMSM with its shaft coupled to a DC generator. A Digital Signal Processor (DSP), *i.e.*, TMS320F28335, joint with a Field Programmable Gate Array (FPGA), *i.e.*, XC3S500E, is used to implement the presented sensorless FOC, with the SOGI-FLL and PWM made in the FPGA and all the other algorithms in the DSP. Phase currents are sampled via an Analog-to-Digital Converter (ADC) build in the DSP and shared with the FPGA via a 16-bit Parallel Bus Interface (PBI). Also placed on the PBI are the position/speed estimates. Computational results are captured with an external Digital-to-Analog Converter (DAC) which has been mapped to the DSP's memory via a Serial Peripheral Interface (SPI). Fig.7 reveals the block diagram of the experimental implementation of the presented method. The switching frequency is 10 kHz, the rotational inertia is 0.12kg·m^2, the DC bus voltage is 320V, and i_o is quantized with a double-sampling technique. Experimental waveforms are recorded with a TPS2024B (Tektronix) oscilloscope.

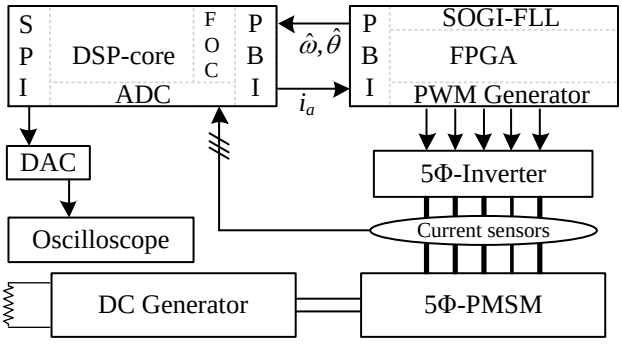

Fig.7 Experimental implementation of the presented method

The control of i_d=0 and i_{q3}=0 is adopted to feed the motor, whereas the torque-current, i_q, is deduced from the speed PI regulator. The low speed limit of the sensorless FOC is around 350rpm below which i_o suffers a low signal-to-noise ratio (SNR). Because of the workload type, the motor is 30% loaded at 350rpm and can be fully loaded at the rated speed. Also, detailed comparisons with the SMO-sensorless-FOC are conducted. Table I is a summary of the 5Φ-PMSM parameters.

Table I
Prototype motor parameters

Symbol	Description	Value
λ_{r1}	1st order rotor flux	0.512Wb
λ_{r3}	3rd order rotor flux	0.034 Wb
R	Resistance per phase	1.1 Ω
P	Pole pair number	2
L_d	d-inductance of 1st subspace	6.54 mH
L_q	q-inductance of 1st subspace	8.32 mH
L_{ls}	Leakage inductance	1.34 mH
	rated speed	1000 rpm
	rated q-current	10A
i_f	current defined in (31)	73A

A. *Free-wheeling current profiles*

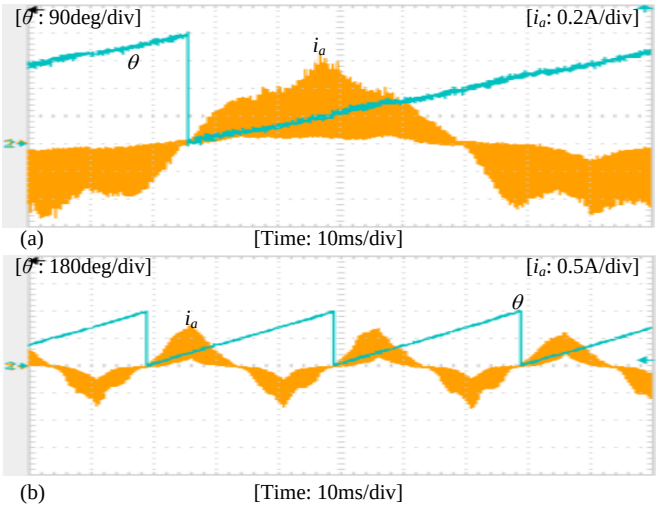

Fig.8 Position and i_a (*i.e.*, -i_o) under: (a) the low-speed limit at 30% load, and (b) the rated speed at full load.

Fig.8 shows the position and the freewheeling current at, respectively, the lower speed limit and rated speed under the presented sensorless FOC. In the figure, i_a (or rather -i_o) is sensed by a current probe, and the noise on its contour is caused by CMV, and hence, a double-sampling technique is suggested. From visual inspection, the zero-crossing point of i_a aligns well with the starting point of the ramped position signal, which agrees with the anticipation of (29) and confirms the correctness of the derived freewheeling current model.

B. *Performance comparisons* (*at the low speed limit*)

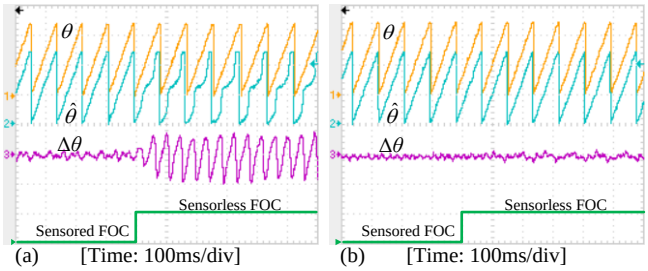

Fig.9 Position and its estimation error in transition from the sensored FOC to the sensorless FOC under: (a) the sliding mode observer-based method, and (b) the presented method. The position and its estimate are scaled to 144deg/div, and $\Delta\theta$ is scaled to 15deg/div.

Fig.9 reveals $\Delta\theta$ ($\Delta\theta = \hat{\theta} - \theta$) oscillation in transition from the sensored FOC to the SMO-sensorless-FOC. The abrupt

switchover in Fig.9 represents a disturbance. Unfortunately, this disturbance eventually brings the system to the edge of oscillation as evident in Fig.9(a). $\Delta\theta$ oscillation in Fig.9(a) is caused by the narrow stability margin of a model-based method, where $\hat{\omega}$ variation eventually triggers the nonlinearity of the state estimator. This drawback can be overcome in the presented sensorless FOC, and as evident in Fig.9(b), the mode transitions more smoothly. To further validate this contention, the speed waveforms during the mode transition are provided.

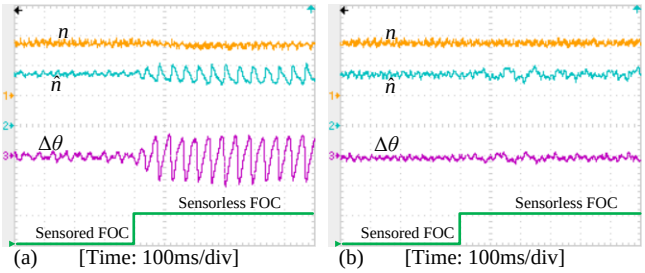

Fig.10 Speed and position estimation error in transition from the sensored FOC to the sensorless FOC under: (a) the sliding mode observer-based method, and (b) the presented method. The speed and its estimate are scaled to 200 rpm/div and $\Delta\theta$ is scaled to 15deg/div.

Fig.10 reveals the speed and $\Delta\theta$ profiles in transition from the sensored FOC to the sensorless FOC under the investigated two philosophies. From Fig.10(a), the speed estimate tightly follows the real speed under the sensored FOC. However, in transitioning to the sensorless FOC, $\Delta\theta$ becomes fluctuating. This is because the minor variation of the speed estimate intensifies the nonlinearity of the state estimator. From 10(b), the speed estimate is also deteriorated after engaging the sensorless FOC, however, $\Delta\theta$ is least impacted. This is because the hardware-based i_o is much more robust against the variation in the speed estimate.

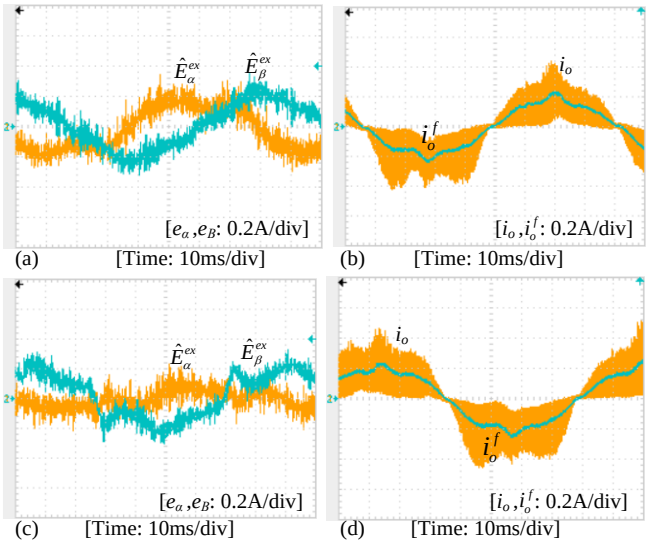

Fig.11 The extended back-EMF estimates and freewheeling currents. (a) The extended back-EMF estimates under a model-based method before engaging the sensorless FOC, (b) freewheeling currents under the presented method before engaging the sensorless FOC, (c) extended back-EMF estimates under a model-based method after engaging the sensorless FOC, and (d) freewheeling currents under the presented method after engaging the sensorless FOC.

Fig.11 shows the back-EMF estimates (or rather, the freewheeling current) before and after engaging the sensorless FOC under two different philosophies. Figs.11(b) and (d), i_o^f represents the fundamental component of the noisy i_o where the unwanted CMV has been filtered out by an LPF. Note that i_o^f, herein, is used for exhibition only. When contrasting Figs.11(a) with (c), the back-EMF estimates become severely distorted after engaging the SMO-sensorless-FOC, and this is because the software back-EMF observer suffers nonlinearities. As a contrast, in Figs.11(b) and (d), i_o rarely changes, regardless of whether the presented sensorless FOC is engaged or not.

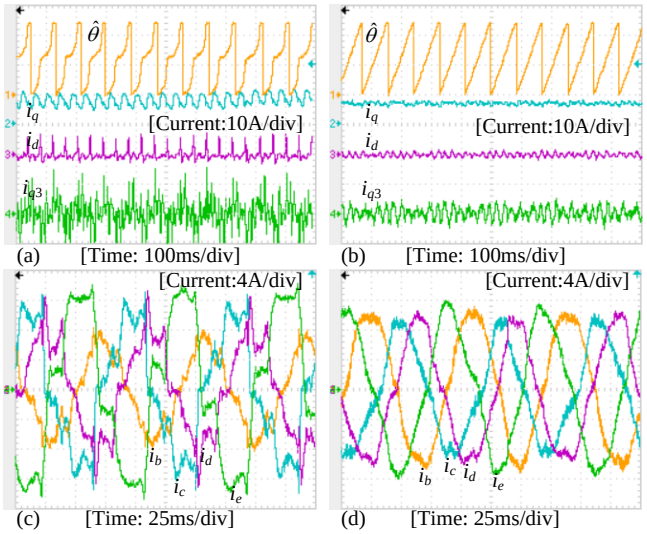

Fig.12 d-q-q_3 frame currents and phase currents. (a) d-q-q_3 frame currents under the SMO-sensorless-FOC, (b) d-q-q_3 frame currents under the presented sensorless FOC, (c) phase currents under the SMO-sensorless-FOC, and (d) phase currents under the presented sensorless FOC. The position estimate is scaled to 144deg/div.

Fig.12 refers to the d-q-q_3 frame currents and the phase currents under the two different sensorless control philosophies. When contrasting Figs.12(a) with (b) as well as Figs.12(c) with (d), the currents under the presented sensorless FOC are more desirable, and its superiority is therefore well proven.

C. *Performance comparisons* (*at the rated speed*)

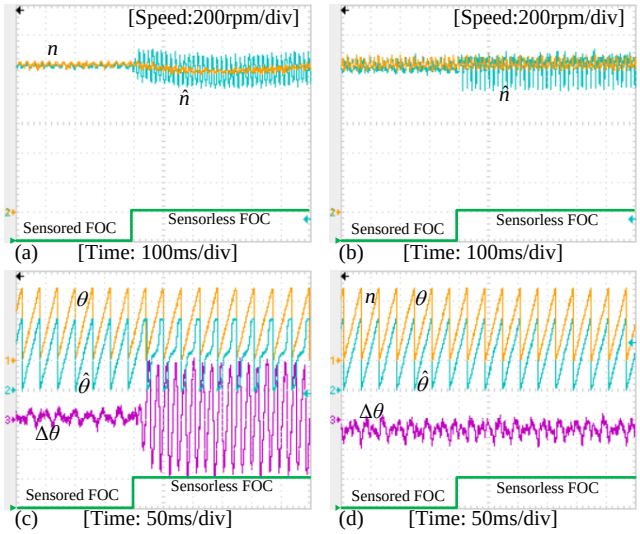

Fig.13 An aggregate of the experimental results at the rated speed in transition from the sensored FOC to the sensorless FOC. (a) Speed and its estimate under SMO-sensorless-FOC, (b) speed and its estimate under the presented sensorless FOC, (c) position and its estimate under the SMO-sensorless-FOC, and (d) position and its estimate under the presented sensorless FOC. The position and its estimate are scaled to 144deg/div, and $\Delta\theta$ is scaled to 15deg/div.

Comparisons with the SMO-sensorless-FOC at the rated

speed are also performed, and Fig.13 shows the corresponding experimental results under the two control philosophies. In both methods, the transition from the sensored FOC to the sensorless FOC could incur oscillation on the speed estimate. However, from Fig.13(c), this oscillation propagates to the back-EMF observer, which further aggravates the oscillation of the position/speed estimate. In the proposed method, this oscillation is blocked at the measurement of i_o, and the position/speed estimate is, therefore, less impacted, as evident in Fig.13(d). Moreover, in Fig.13(d), the mode transitions smoothly and $\Delta\theta$ rarely changes, and this confirms the superiority of the presented method at the rated speed.

D. Anti-disturbance performance of the presented method

As demonstrated above, the SMO-sensorless-FOC is subject to a slow dynamic and can oscillate or may even fail facing disturbances. In contrast, the presented sensorless FOC is more functional. Therefore, in this section, only the presented method is evaluated by exerting certain external or internal disturbances. Additionally, for a successful sensorless FOC, the bandwidth of the speed PI controller should be narrowed. This implies the dynamic response of a sensorless FOC is slower than the sensored FOC, because the sensorless FOC always uses filters to improve the SNR.

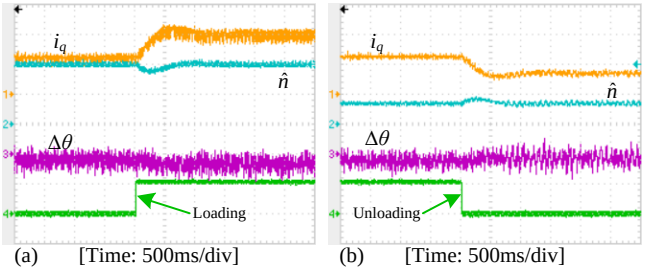

(a) [Time: 500ms/div] (b) [Time: 500ms/div]

Fig.14 Sensorless FOC in response to abruptly loading/unloading. (a) the motor is fully loaded at rated speed, and (b)The motor is unloaded at 350 rpm. i_q is scaled to 5A/div, the speed estimate is scaled to 500rpm, and $\Delta\theta$ is scaled to 15deg/div.

Fig.14 refers to the presented sensorless FOC under abruptly loading/unloading at, respectively, the lower and upper speed limits. This is to evaluate the robustness of the proposed sensorless FOC against the external disturbance. Fig.14(a) shows the responses of, respectively, the speed estimate, i_q, and $\Delta\theta$ against abruptly loading. Note that at the rated speed, unloading action will bring the sensorless FOC to the overmodulation region and thus shall be avoided. From Fig.14(a), the motor resettles to the speed setpoint in 1.2s, and as anticipated, $\Delta\theta$ increased slightly in this process. Fig.14(b) shows waveforms of the speed estimate, i_q, and $\Delta\theta$ in response to abruptly unloading. Also note that at this low-speed limit, loading action will bring the sensorless FOC to the failure region which shall also be avoided. The low-speed limit, 350rpm, is obtained by experimental trials, and below this speed, the sensorless FOC may fail because the extended rotor flux is corrupted by the dynamic of i_q.

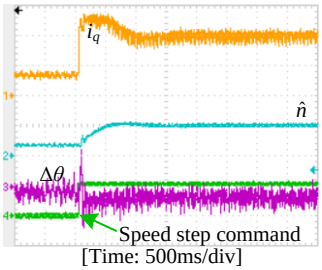

[Time: 500ms/div]

Fig.15 Step response and $\Delta\theta$ trend while driving the motor from 350rpm to 1000rpm under the presented sensorless FOC. i_q is scaled to 5A/div, speed estimate is scaled to 1000rpm, and $\Delta\theta$ is scaled to 15deg/div.

Fig.15 refers to the step response and $\Delta\theta$ trend while driving the motor from 350rpm to 1000rpm under the presented sensorless FOC. Limited to the workload type, the motor is initially set at 350rpm with 30% load, and after a step command is initiated at 1s, the motor is brought to a fully loaded condition. During the first 1s, $\Delta\theta$ is within 5°. Then, $\Delta\theta$ experiences a shortly damped oscillation immediately after issuing the step command, and this oscillation is supposed to be caused by the dynamic of i_q. As the motor gets fully loaded, $\Delta\theta$ increases up to 12°. The position estimation error agrees with that anticipated, and the validity of the proposed sensorless FOC is therefore confirmed. This test also suggests that abrupt change of i_q could incur some oscillation on $\Delta\theta$, which is in line with the analytical model. Fortunately, this oscillation is damped swiftly and does not lead to any system abnormalities, which proves the robustness of the proposed sensorless control.

In summary, the presented sensorless FOC is efficient in dynamic response, and it is less parameterized and more functional in comparison to a model-based method.

VI. CONCLUSIONS

This paper proposes a brand-new sensorless control for a generic 5Φ-PMSM under the single-phase IGBT failures by exploiting the freewheeling current in the failed phase. In this work, the freewheeling current is firstly modeled and theoretically proved to carry the back-EMF information. Based on this model, a single SOGI-FLL is suggested to extract the position/speed estimates. The proposed method is experimentally evaluated at the mid-high speeds with capabilities to withstand non-frequently varying internal/external disturbances. The proposed sensorless control is less parameterized and is featured on an improved dynamic relative to a model-based method, and it can be best suitable for a 5Φ-PMSM under the single-phase IGBT failures.

Besides this, in the healthy mode, it is possible to deliberately switch off one IGBT-bridge to create the IGBT failure environment so the presented sensorless FOC is still applicable, with, however, a power derating. The contention is whether the benefit of an improved dynamic overweighs its disadvantage of the power derating. Comprehensive comparisons in this respect will be performed in the future.

REFERENCES

[1] F. Barrero and M. J. Duran, "Recent Advances in the Design, Modeling, and Control of Multiphase Machines—Part I," *IEEE Transactions on Industrial Electronics*, vol. 63, no. 1, pp. 449-458, 2016, doi: 10.1109/TIE.2015.2447733.

[2] J. K. Nøland, M. Leandro, J. A. Suul, and M. Molinas, "High-Power Machines and Starter-Generator Topologies for More Electric Aircraft: A Technology Outlook," *IEEE Access*, pp. 1-1, 2020, doi: 10.1109/ACCESS.2020.3007791.

[3] S. He, Z. Xu, M. Chen, H. Yang, and W. Li, "General Derivation Law with Torque-Free Achieving of Integral On-Board Charger on Compact Powertrains," *IEEE Transactions on Industrial Electronics*, pp. 1-1, 2020, doi: 10.1109/TIE.2020.3005063.

[4] A. D. Pizzo, L. P. D. Noia, and A. Pizza, "Analysis of a five phase electrical drive for the propulsion of all electric aircraft," in *2016 AEIT International Annual Conference (AEIT)*, 5-7 Oct. 2016 2016, pp. 1-6, doi: 10.23919/AEIT.2016.7892785.

[5] F. Scuiller, H. Zahr, and E. Semail, "A bi-harmonic five-phase SPM machine with low ripple torque for marine propulsion," in *2017 IEEE International Electric Machines and Drives Conference (IEMDC)*, 21-24 May 2017 2017, pp. 1-7, doi: 10.1109/IEMDC.2017.8002259.

[6] M. J. Duran and F. Barrero, "Recent Advances in the Design, Modeling, and Control of Multiphase Machines—Part II," *IEEE Transactions on Industrial Electronics*, vol. 63, no. 1, pp. 459-468, 2016, doi: 10.1109/TIE.2015.2448211.

[7] L. Zhang, X. Zhu, J. Gao, and Y. Mao, "Design and Analysis of New Five-Phase Flux-Intensifying Fault-Tolerant Interior-Permanent-Magnet Motor for Sensorless Operation," *IEEE Transactions on Industrial Electronics*, vol. 67, no. 7, pp. 6055-6065, 2020, doi: 10.1109/TIE.2019.2955407.

[8] P. Zheng, Y. Sui, J. Zhao, C. Tong, T. A. Lipo, and A. Wang, "Investigation of a Novel Five-Phase Modular Permanent-Magnet In-Wheel Motor," *IEEE Transactions on Magnetics*, vol. 47, no. 10, pp. 4084-4087, 2011, doi: 10.1109/TMAG.2011.2150207.

[9] W. Huang, W. Hua, F. Chen, J. Qi, and J. Zhu, "Performance Improvement of Model Predictive Current Control of Fault-Tolerant Five-Phase Flux-Switching Permanent Magnet Motor Drive," *IEEE Transactions on Industry Applications*, vol. 55, no. 6, pp. 6001-6010, 2019, doi: 10.1109/TIA.2019.2935424.

[10] L. Zhang, Y. Fan, R. Cui, R. D. Lorenz, and M. Cheng, "Fault-Tolerant Direct Torque Control of Five-Phase FTFSCW-IPM Motor Based on Analogous Three-Phase SVPWM for Electric Vehicle Applications," *IEEE Transactions on Vehicular Technology*, vol. 67, no. 2, pp. 910-919, 2018, doi: 10.1109/TVT.2017.2760980.

[11] B. Tian, Q. An, J. Duan, D. Sun, L. Sun, and D. Semenov, "Decoupled Modeling and Nonlinear Speed Control for Five-Phase PM Motor Under Single-Phase Open Fault," *IEEE Transactions on Power Electronics*, vol. 32, no. 7, pp. 5473-5486, 2017, doi: 10.1109/TPEL.2016.2611532.

[12] H. Guzman *et al.*, "Comparative Study of Predictive and Resonant Controllers in Fault-Tolerant Five-Phase Induction Motor Drives," *IEEE Transactions on Industrial Electronics*, vol. 63, no. 1, pp. 606-617, 2016, doi: 10.1109/TIE.2015.2418732.

[13] H. Zhou, W. Zhao, G. Liu, R. Cheng, and Y. Xie, "Remedial Field-Oriented Control of Five-Phase Fault-Tolerant Permanent-Magnet Motor by Using Reduced-Order Transformation Matrices," *IEEE Transactions on Industrial Electronics*, vol. 64, no. 1, pp. 169-178, 2017, doi: 10.1109/TIE.2016.2599501.

[14] J. Zhang, W. Zhan, and M. Ehsani, "Fault-Tolerant Control of PMSM With Inter-Turn Short-Circuit Fault," *IEEE Transactions on Energy Conversion*, vol. 34, no. 4, pp. 2267-2275, 2019, doi: 10.1109/TEC.2019.2936225.

[15] I. Jlassi, J. O. Estima, S. K. E. Khil, N. M. Bellaaj, and A. J. M. Cardoso, "A Robust Observer-Based Method for IGBTs and Current Sensors Fault Diagnosis in Voltage-Source Inverters of PMSM Drives," *IEEE Transactions on Industry Applications*, vol. 53, no. 3, pp. 2894-2905, 2017, doi: 10.1109/TIA.2016.2616398.

[16] H. Guzman, F. Barrero, and M. J. Duran, "IGBT-Gating Failure Effect on a Fault-Tolerant Predictive Current-Controlled Five-Phase Induction Motor Drive," *IEEE Transactions on Industrial Electronics*, vol. 62, no. 1, pp. 15-20, 2015, doi: 10.1109/TIE.2014.2331019.

[17] D. Lee and K. Akatsu, "The Study on Position Sensor Fault Detection and Algorithm Transition from Sensored to Sensorless Control for IPMSM," in *2019 10th International Conference on Power Electronics and ECCE Asia*, 27-30 May 2019 2019, pp. 1-6.

[18] G. H. B. Foo, X. Zhang, and D. M. Vilathgamuwa, "A Sensor Fault Detection and Isolation Method in Interior Permanent-Magnet Synchronous Motor Drives Based on an Extended Kalman Filter," *IEEE Transactions on Industrial Electronics*, vol. 60, no. 8, pp. 3485-3495, 2013, doi: 10.1109/TIE.2013.2244537.

[19] G. Zhang, H. Zhou, G. Wang, C. Li, and D. Xu, "Current Sensor Fault Tolerant Control for Encoderless IPMSM Drives Based on Current Space Vector Error Reconstruction," *IEEE Journal of Emerging and Selected Topics in Power Electronics*, pp. 1-1, 2019.

[20] G. Zhang, G. Wang, H. Wang, D. Xiao, L. Li, and D. Xu, "Pseudorandom-Frequency Sinusoidal Injection Based Sensorless IPMSM Drives With Tolerance for System Delays," *IEEE Transactions on Power Electronics*, vol. 34, no. 4, pp. 3623-3632, 2019, doi: 10.1109/TPEL.2018.2865802.

[21] L. Parsa and H. A. Toliyat, "Sensorless Direct Torque Control of Five-Phase Interior Permanent-Magnet Motor Drives," *IEEE Transactions on Industry Applications*, vol. 43, no. 4, pp. 952-959, 2007.

[22] F. Briz, M. W. Degner, P. G. Fernandez, and A. B. Diez, "Rotor and flux position estimation in delta-connected AC Machines using the zero-sequence carrier-signal current," *IEEE Transactions on Industry Applications*, vol. 42, no. 2, pp. 495-503, 2006, doi: 10.1109/TIA.2006.870046.

[23] P. L. Xu and Z. Q. Zhu, "Novel Carrier Signal Injection Method Using Zero-Sequence Voltage for Sensorless Control of PMSM Drives," *IEEE Transactions on Industrial Electronics*, vol. 63, no. 4, pp. 2053-2061, 2016, doi: 10.1109/TIE.2015.2506146.

[24] Y. Yoon, S. Sul, S. Morimoto, and K. Ide, "High-Bandwidth Sensorless Algorithm for AC Machines Based on Square-Wave-Type Voltage Injection," *IEEE Transactions on Industry Applications*, vol. 47, no. 3, pp. 1361-1370, 2011, doi: 10.1109/TIA.2011.2126552.

[25] B. Tian, Q. An, and M. Molinas, "High-Frequency Injection-Based Sensorless Control for a General Five-Phase BLDC Motor Incorporating System Delay and Phase Resistance," *IEEE Access*, vol. 7, pp. 162862-162873, 2019, doi: 10.1109/ACCESS.2019.2950256.

[26] G. Liu, C. Geng, and Q. Chen, "Sensorless Control for Five-Phase IPMSM Drives by Injecting HF Square-Wave Voltage Signal into Third Harmonic Space," *IEEE Access*, vol. 8, pp. 69712-69721, 2020, doi: 10.1109/ACCESS.2020.2986347.

[27] L. Zhang, Y. Fan, C. Li, A. Nied, and M. Cheng, "Fault-Tolerant Sensorless Control of a Five-Phase FTFSCW-IPM Motor Based on a Wide-Speed Strong-Robustness Sliding Mode Observer," *IEEE Transactions on Energy Conversion*, vol. 33, no. 1, pp. 87-95, 2018, doi: 10.1109/TEC.2017.2727074.

[28] Q. Lu, X. Zhu, L. Quan, Y. Zuo, and S. Du, "Rotor position estimation scheme with harmonic ripple attenuation for sensorless controlled permanent magnet synchronous motors," *IET Electric Power Applications*, vol. 12, no. 8, pp. 1200-1206, 2018, doi: 10.1049/iet-epa.2017.0858.

[29] G. Zhang, G. Wang, D. Xu, and N. Zhao, "ADALINE-Network-Based PLL for Position Sensorless Interior Permanent Magnet Synchronous Motor Drives," *IEEE Transactions on Power Electronics*, vol. 31, no. 2, pp. 1450-1460, 2016, doi: 10.1109/TPEL.2015.2424256.

[30] Y. Wang, Y. Xu, and J. Zou, "ILC-Based Voltage Compensation Method for PMSM Sensorless Control Considering Inverter Nonlinearity and Sampling Current DC Bias," *IEEE Transactions on Industrial Electronics*, vol. 67, no. 7, pp. 5980-5989, 2020, doi: 10.1109/TIE.2019.2921289.

[31] Q. An, J. Zhang, Q. An, and A. Shamekov, "Quasi-Proportional-Resonant Controller Based Adaptive Position Observer for Sensorless Control of PMSM Drives Under Low Carrier Ratio," *IEEE Transactions on Industrial Electronics*, vol. 67, no. 4, pp. 2564-2573, 2020.

[32] G. Wang, R. Yang, and D. Xu, "DSP-Based Control of Sensorless IPMSM Drives for Wide-Speed-Range Operation," *IEEE Transactions on Industrial Electronics*, vol. 60, no. 2, pp. 720-727, 2013, doi: 10.1109/TIE.2012.2205360.

[33] B. Tian, L. Sun, M. Molinas, and Q. An, "Repetitive control-based phase voltage modulation amendment for FOC-based five-phase PMSMs under single-phase open fault," *IEEE Transactions on Industrial Electronics*, pp. 1-1, 2020, doi: 10.1109/TIE.2020.2975502.

[34] L. Parsa and H. A. Toliyat, "Five-phase permanent-magnet motor drives," *IEEE Transactions on Industry Applications*, vol. 41, no. 1, pp. 30-37, 2005, doi: 10.1109/TIA.2004.841021.

[35] G. Wang *et al.*, "Enhanced Position Observer Using Second-Order Generalized Integrator for Sensorless Interior Permanent Magnet Synchronous Motor Drives," *IEEE Transactions on Energy Conversion*, vol. 29, no. 2, pp. 486-495, 2014, doi: 10.1109/TEC.2014.2311098.

[36] S. Golestan, J. M. Guerrero, J. C. Vasquez, A. M. Abusorrah, and Y. Al-Turki, "Modeling, Tuning, and Performance Comparison of Second-Order-Generalized-Integrator-Based FLLs," *IEEE Transactions on Power Electronics*, vol. 33, no. 12, pp. 10229-10239, 2018, doi: 10.1109/TPEL.2018.2808246.

[37] C. Zhang, X. Cai, A. Rygg, and M. Molinas, "Sequence Domain SISO Equivalent Models of a Grid-Tied Voltage Source Converter System for Small-Signal Stability Analysis," *IEEE Transactions on Energy Conversion*, vol. 33, no. 2, pp. 741-749, 2018, doi: 10.1109/TEC.2017.2766217.